

PAINT: Pathology-Aware Integrated Next-Scale Transformation for Virtual Immunohistochemistry

Rongze Ma, Mengkang Lu, Zhenyu Xiang, Yongsheng Pan, Yicheng Wu, Qingjie Zeng, Yong Xia *Member, IEEE*

Abstract—Virtual immunohistochemistry (IHC) aims to computationally synthesize molecular staining patterns from routine Hematoxylin and Eosin (H&E) images, offering a cost-effective and tissue-efficient alternative to traditional physical staining. However, this task is particularly challenging: H&E morphology provides ambiguous cues about protein expression, and similar tissue structures may correspond to distinct molecular states. Most existing methods focus on direct appearance synthesis to implicitly achieve cross-modal generation, often resulting in semantic inconsistencies due to insufficient structural priors. In this paper, we propose Pathology-Aware Integrated Next-Scale Transformation (PAINT), a visual autoregressive framework that reformulates the synthesis process as a structure-first conditional generation task. Unlike direct image translation, PAINT enforces a causal order by resolving molecular details conditioned on a global structural layout. Central to this approach is the introduction of a Spatial Structural Start Map (3S-Map), which grounds the autoregressive initialization in observed morphology, ensuring deterministic, spatially aligned synthesis. Experiments on the IHC4BC and MIST datasets demonstrate that PAINT outperforms state-of-the-art methods in structural fidelity and clinical downstream tasks, validating the potential of structure-guided autoregressive modeling.

Index Terms—Visual Autoregressive Modeling, Virtual Immunohistochemistry, Computational Pathology

I. INTRODUCTION

Immunohistochemistry (IHC) is a fundamental tool in modern pathological diagnosis, enabling the visualization of protein expression patterns that guide tumor subtyping, prognostic assessment, and decision-making [1], [2]. Despite its clinical importance, IHC remains resource-intensive, requiring additional tissue sections and specialized reagents. These limitations are particularly restrictive when tissue availability is scarce or rapid diagnostic turnaround is required. Consequently, there has been growing interest in virtual IHC, which aims to generate IHC staining patterns directly from routine Hematoxylin and Eosin (H&E) slides [3], [4].

This work was supported in part by the National Natural Science Foundation of China under Grant 92470101 and Grant 62401475. (R. Ma and M. Lu contributed equally to this work.) (Corresponding authors: Qingjie Zeng and Yong Xia.)

R. Ma, M. Lu, Z. Xiang, Y. Pan, Q. Zeng, and Y. Xia are with School of Computer Science and Engineering, Northwestern Polytechnical University, Xi'an 710072, China (e-mail: {rongzema129, lmk, xiangzy, qjzeng}@mail.nwpu.edu.cn; {yspan, yxia}@nwpu.edu.cn).

Y. Wu is with Monash University, Clayton, VIC 3168, Australia (e-mail: yicheng.wu@monash.edu).

Virtual IHC poses a fundamentally ill-posed inference problem. While H&E images encode tissue morphology and cellular organization, IHC reveals molecular expression that is only indirectly reflected in morphology [5], [6]. The relationship between H&E morphology and protein expression is inherently ambiguous and underdetermined: morphologically similar regions may correspond to distinct molecular states due to differences in cellular composition, microenvironment, or disease progression [7]. This intrinsic uncertainty implies that virtual IHC cannot be treated as a deterministic modality translation task. Instead, it is a conditional generation task that requires hierarchical reasoning, where global structural context must be established before resolving local molecular patterns. This hierarchical reasoning mirrors clinical practice, in which pathologists first interpret coarse architectural cues (e.g., tumor boundaries, glandular organization, and stromal interfaces) to contextualize subsequent assessment of molecular markers at finer scales. Consistently, IHC expression patterns are largely governed by region-level cellular composition and microenvironmental context, which must be inferred at a coarse scale prior to synthesizing fine-grained molecular details under incomplete morphological constraints [8], [9].

Most existing virtual staining methods formulate the task as deterministic image-to-image (I2I) translation, commonly adopting general-purpose frameworks such as Pix2Pix [10] and CycleGAN [11]. However, directly transferring these objectives to pathology can be problematic, as pixel-level reconstruction and cycle-consistency losses lack pathology-specific semantic constraints and often prioritize visual realism over biological plausibility. This can lead to *structural hallucination*, where marker positivity or negativity is incorrectly assigned across regions that are visually similar but biologically distinct (e.g., false positivity outside tumor nests), yielding spatially inconsistent yet visually plausible staining patterns [12]–[15]. Recent works have attempted to alleviate this issue by introducing pathology-aware constraints, such as contrastive alignment or semantic preservation losses [7], [16]. While these strategies improve local correspondence, they remain within a deterministic translation paradigm and primarily regulate appearance or patch-level fidelity, without explicitly enforcing region-level structural consistency between H&E and IHC. This limitation contrasts with clinical pathology principles, where molecular signals are expected to remain spatially coherent with tissue compartments and architectural organization [9].

These observations motivate a shift from deterministic trans-

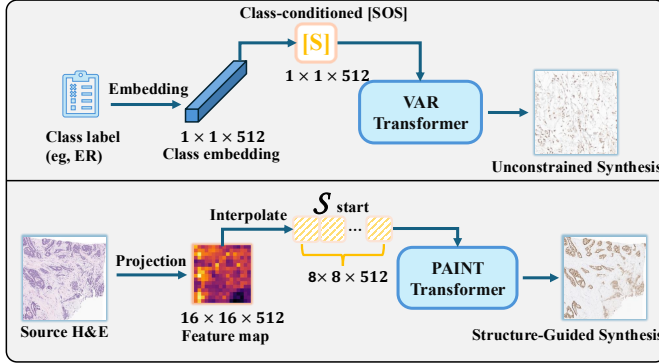


Fig. 1. Standard VAR (top) relies on a generic token (Start of Sequence [SOS]) lacking morphological grounding. In contrast, PAINT (bottom) introduces a **Spatial Structural Start Map** (S_{start})—a dense feature prior synthesized from the H&E image—that strictly aligns the autoregressive synthesis with the source morphology.

lation toward hierarchical generative modeling. The recently developed visual autoregressive models (VAR) [17] offer a promising alternative by generating images in a coarse-to-fine manner, first generating low-resolution latent representations and then progressively refining high-resolution details conditioned on this coarse context [18]. Such generation order aligns naturally with pathological reasoning, which prioritizes global tissue architecture before focusing on cellular-level interpretation [9]. However, directly applying VAR to pathology images remains challenging. In the absence of explicit spatial anchoring to the source H&E morphology, early generative decisions lack a morphology-grounded structural hypothesis to condition subsequent refinement, leading to spatial drift and error accumulation during autoregressive synthesis [19] (Fig. 1, top). Consequently, ensuring precise spatial alignment and reducing anatomically implausible layouts remains a critical challenge, since the model must infer molecular signals while strictly adhering to the spatial constraints of the source morphology.

To address these challenges, we propose **Pathology-Aware Integrated Next-Scale Transformation** (PAINT), a VAR framework tailored for virtual IHC. Unlike standard VAR that relies on a generic [SOS] token for class-conditional generation, PAINT introduces a dual-constrained **Spatial Structural Start Map** (3S-Map) that enforces feature alignment in both the latent space and the image space, providing an IHC-aligned spatial prior for initializing autoregressive synthesis (see Fig. 1, bottom). Specifically, PAINT operates in three stages. First, PAINT separately trains two VQ-VAEs on H&E and IHC images to learn hierarchical, modality-specific discrete token maps [20], thereby establishing dedicated perceptual vocabularies for tissue morphology and molecular staining patterns. Second, PAINT trains a cross-modal Translator that projects frozen H&E latent representations into the continuous IHC feature space via Latent-Space Alignment (LSA) and Image-Space Alignment (ISA), explicitly enforcing semantic and spatial consistency across modalities. Finally, the aligned features are interpolated to construct the *3S-Map*, which initializes the autoregressive generation trajectory and serves as an IHC-aligned spatial prior, guiding subsequent visual

autoregressive synthesis toward anatomically coherent layouts while progressively rendering IHC-specific molecular textures. Through this design, PAINT achieves state-of-the-art (SOTA) performance on the IHC4BC¹ and MIST datasets, improving both visual fidelity and clinically relevant prediction accuracy.

Our main contributions are threefold:

- We propose **PAINT**, a pathology-aware VAR framework for virtual IHC that incorporates explicit spatial structural priors into synthesis, enabling pathology-consistent cross-modal generation guided by tissue morphology.
- We introduce a **3S-Map** that is jointly constrained in the latent and image spaces via LSA and ISA, providing an IHC-aligned spatial prior that mitigates region-level structural shift during autoregressive synthesis.
- Experiments on the IHC4BC and MIST datasets show that PAINT consistently outperforms existing methods in both image quality and downstream clinical tasks.

II. RELATED WORK

A. Generative Models for Image Synthesis and Translation

I2I translation aims to learn mappings between source and target images while preserving structural content. Pix2Pix [10] uses conditional GANs for supervised translation with paired data, but it struggles with medical imaging due to the need for precise pixel-level correspondence. To address this, CycleGAN [11] introduces cycle-consistency for unpaired translation. However, CycleGAN’s reliance on strict cycle-consistency can be problematic in medical imaging, where complex or weakly labeled relationships may lead to inaccurate translations and fail to capture nuanced morphological-molecular correlations. To mitigate these issues, CUT [21] utilizes contrastive learning to promote patch-level correspondence, improving weakly-labeled scenarios. Recent diffusion models, including SynDiff [22] and latent diffusion models (LDMs) [23], have shown promising results through iterative denoising for improved quality and stability. Despite these advances, these methods continue to treat cross-modal synthesis mainly as style transfer, lacking mechanisms to enforce the global semantic and structural consistency needed for accurate medical interpretations. Autoregressive generative models, such as VQ-VAEs, model images as sequences of discrete latent tokens, learning compact and semantically meaningful representations that separate high-level structure from low-level appearance [24]–[26]. But conventional raster-scan autoregressive generation is computationally inefficient and may disrupt spatial coherence [27], [28]. Recent VAR modeling addresses these limitations through next-scale prediction, generating images progressively from coarse layouts to fine details [17]. By explicitly encoding multi-scale spatial hierarchy, VAR offers a structured and spatially grounded generation strategy.

¹<https://www.kaggle.com/datasets/akbarnejad1991/ihc4bc-compressed>

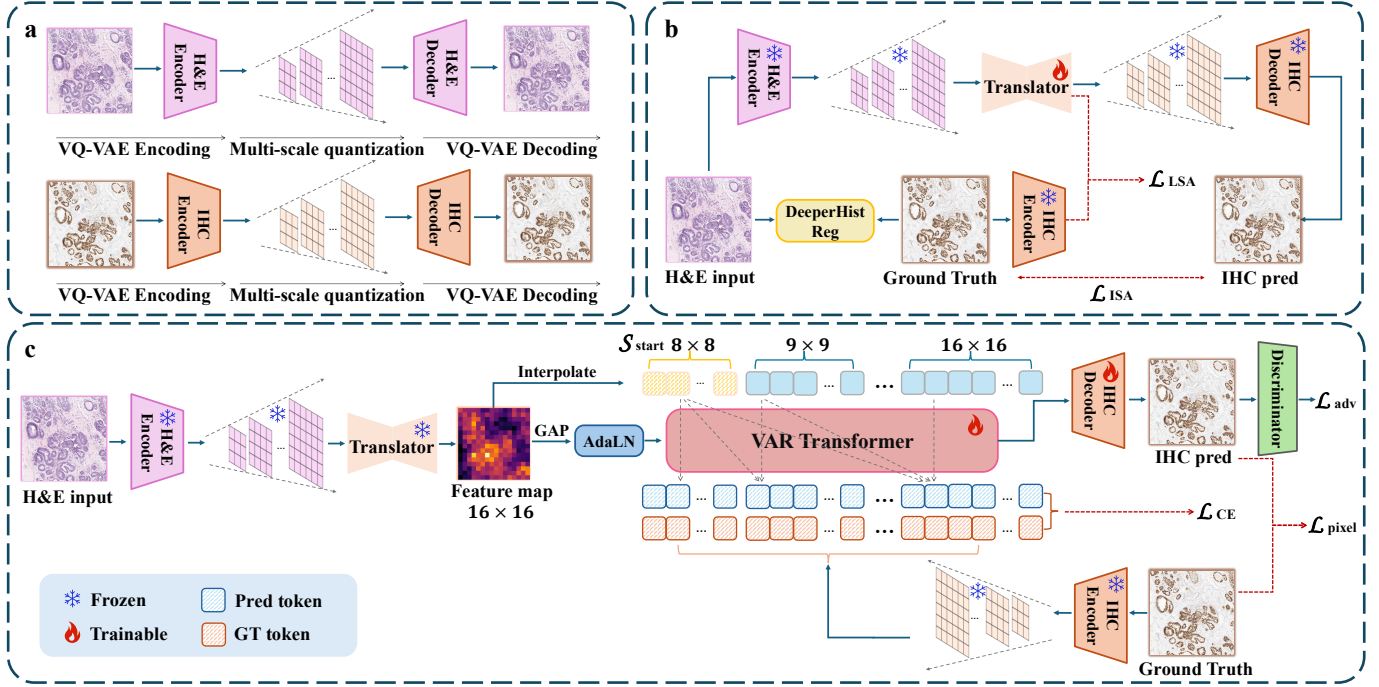


Fig. 2. Overview of the proposed PAINT framework. (a) PAINT independently trains two domain-specific multi-scale VQ-VAEs for H&E and IHC images. Each encoder maps the input image to continuous latent features, which are discretized into hierarchical token maps via residual vector quantization. The corresponding decoders reconstruct the images to ensure compact yet high-fidelity representations. After training, all VQ-VAE encoders and decoders are frozen. (b) Using paired H&E-IHC samples registered by DeeperHistReg, a translation network (U-Net) maps H&E latent features, extracted by the frozen H&E encoder, into the continuous IHC feature space. This stage is supervised by LSA for feature consistency and ISA via the frozen IHC decoder for reconstruction fidelity, producing spatially aligned and structurally consistent intermediate representations. (c) A Visual Autoregressive (VAR) Transformer progressively predicts IHC token maps in a coarse-to-fine, next-scale manner. Translated features are injected as structural conditions via Adaptive Layer Normalization (AdaLN), guiding the autoregressive process to preserve tissue morphology while synthesizing realistic molecular textures. The final IHC image is reconstructed by the IHC VQ-VAE decoder.

B. Virtual Staining in Computational Pathology

To ensure effective visual staining in pathology, many existing methods introduce pathology-specific constraints. Specifically, ASP [29] introduces adaptive PatchNCE loss to reduce sensitivity to alignment issues, while PPT [16] uses bidirectional contrastive learning with patch alignment loss to address misalignment in paired images. However, both focus mainly on patch-level consistency and still struggle with global semantic alignment, especially in regions with severe misalignment. PSPStain [7] improves molecular specificity by modeling protein expression with optical density estimation and prototype consistency learning. While effective in preserving molecular semantics, its performance depends on the quality of these strategies, particularly when dealing with spatial misalignment. HistDiST [30] applies latent diffusion with dual morphological conditioning to enhance structural and molecular fidelity, but its reliance on base models for inference limits flexibility and fine-tuning for diverse molecular features. Despite these advances, most virtual IHC staining methods prioritize pixel- or patch-level alignment while neglecting the crucial role of structural priors in capturing spatial relationships among tissue regions. This absence of structure-aware modeling undermines their ability to maintain consistent tissue organization.

III. METHODOLOGY

A. Overview

Fig. 2 illustrates the overall PAINT framework, which enables H&E-to-IHC synthesis by explicitly injecting structural priors into a next-scale transformation architecture. The framework consists of three stages. In the first stage, PAINT trains two VQ-VAE models to reconstruct H&E and IHC images, respectively, aiming to initialize modality-specific representations. In the second stage, PAINT learns a feature-level translation from the H&E latent space to the IHC latent space using paired, spatially registered samples, guided by specially designed ISA and LSA loss constraints to enforce structurally consistent cross-modality correspondences. In the final stage, PAINT performs virtual staining through next-scale autoregressive generation, explicitly conditioned on the translated structural prior and a hierarchical generation scheme, thereby anchoring molecular synthesis to patient-specific tissue morphology.

B. Initialization of modality-specific visual perception

To model the substantial appearance and distributional differences between H&E and IHC images, PAINT first trains two parallel VQ-VAE models, denoted as VQ_{HE} and VQ_{IHC} . We adopt the multi-scale residual quantization paradigm of VQ-VAE2 [18]. Specifically, each image is represented as a pyramid of K discrete latent grids with increasing spatial resolutions, ranging from (8×8) to (16×16) . The models VQ_{HE}

and VQ_{IHC} are trained independently with separate codebooks, \mathcal{Z}_{HE} and \mathcal{Z}_{IHC} , allowing modality-specific appearance statistics to be faithfully preserved. Since the training procedures of VQ_{HE} and VQ_{IHC} are identical, we describe only the VQ_{HE} branch for brevity. Given an input image X , the encoder \mathcal{E} produces a continuous feature map $f = \mathcal{E}(X)$. Multi-scale quantization is concurrently performed in a residual manner. At scale k , the residual feature $f_{res}^{(k)}$ is interpolated to resolution $h_k \times w_k$ and quantized via nearest-neighbor lookup:

$$\begin{aligned} r_k &= \mathcal{Q}(\text{Interpolate}(f_{res}^{(k)}, h_k, w_k)), \\ z_k &= \text{lookup}(\mathcal{Z}_{HE}, r_k), \end{aligned} \quad (1)$$

Here, $\mathcal{Q}(\cdot)$ denotes a nearest-neighbor vector quantizer that, at each spatial location, assigns the interpolated residual feature vector to the index of its closest codeword in the codebook \mathcal{Z}_{HE} under the Euclidean distance. The residual feature is then updated to preserve information not captured at the current scale:

$$f_{res}^{(k+1)} = f_{res}^{(k)} - \phi_k(\text{Interpolate}(z_k, H, W)), \quad (2)$$

where $f_{res}^{(1)}$ is initialized as the original encoder feature f , ϕ_k denotes a scale-specific projection and (H, W) is the resolution of f . The aggregated quantized feature map \hat{f} is formed by accumulating the projected features from all scales:

$$\hat{f} = \sum_{k=1}^K \phi_k(\text{Interpolate}(z_k, H, W)), \quad (3)$$

Both VQ_{HE} and VQ_{IHC} are trained using the bitwise loss [31], which incorporates reconstruction \mathcal{L}_{rec} , semantic \mathcal{L}_{feat} , perceptual \mathcal{L}_P [32], and realism constraints \mathcal{L}_{adv} [10], formulated as:

$$\mathcal{L} = \underbrace{\|X - \hat{X}\|_1}_{\mathcal{L}_{rec}} + \underbrace{\|f - \hat{f}\|_1}_{\mathcal{L}_{feat}} + \lambda_p \mathcal{L}_P(X, \hat{X}) + \lambda_{adv} \mathcal{L}_{adv}(X, \hat{X}), \quad (4)$$

where $\hat{X} = \mathcal{D}(\hat{f})$ is the reconstructed image produced by the decoder \mathcal{D} .

C. Feature Alignment for 3S-Map Initialization

To prepare the structural prior for H&E-to-IHC translation, PAINT performs a feature-space mapping from H&E to IHC using paired images registered with DeeperHistReg [33]. Given an H&E image X_{HE} , PAINT extracts its aggregated quantized feature map \hat{f}_{HE} using the pre-trained VQ_{HE} . A translation network \mathcal{T} that utilizes a U-Net backbone [34] is then employed to map \hat{f}_{HE} to a continuous IHC feature prediction:

$$f_{IHC}^{pred} = \mathcal{T}(\hat{f}_{HE}), \quad (5)$$

where f_{IHC}^{pred} is the predicted latent feature from H&E space. To achieve the desired structural consistency, two alignment strategies are introduced.

LSA. To ensure accurate projection from H&E to IHC in the latent space, we introduce a LSA loss that minimizes the ℓ_1 distance between f_{IHC}^{pred} and f_{IHC}^{gt} , where f_{IHC}^{gt} is obtained by

Algorithm 1: Multi-scale VQ-VAE Encoding and Reconstruction (H&E or IHC)

Inputs: raw image X ;
Hyperparameters: number of scales K , resolutions $(h_k, w_k)_{k=1}^K$;

1 Encoding: Multi-scale Residual Quantization

2 $f = \mathcal{E}(X)$;

3 $f_{res}^{(1)} = f$;

4 $R = []$;

5 **for** $k = 1, \dots, K$ **do**

6 $r_k = \mathcal{Q}(\text{Interpolate}(f_{res}^{(k)}, h_k, w_k))$;

7 $R \leftarrow \text{queue_push}(R, r_k)$;

8 $z_k = \text{lookup}(\mathcal{Z}, r_k)$;

9 $f_{res}^{(k+1)} = f_{res}^{(k)} - \phi_k(\text{Interpolate}(z_k, H, W))$;

10 Reconstruction: Multi-scale Feature Aggregation

11 $\hat{f}^{(1)} = 0$;

12 **for** $k = 1, \dots, K$ **do**

13 $r_k = \text{queue_pop}(R)$;

14 $z_k = \text{lookup}(\mathcal{Z}, r_k)$;

15 $\hat{f}^{(k+1)} = \hat{f}^{(k)} + \phi_k(\text{Interpolate}(z_k, H, W))$;

16 Decoding

17 $\hat{X} = \mathcal{D}(\hat{f}^{(K+1)})$;

Return: reconstructed image \hat{X} ; multi-scale tokens R ;

encoding the registered ground-truth IHC image X_{IHC} using the pre-trained VQ_{IHC} encoder. Formally,

$$\mathcal{L}_{LSA} = \|f_{IHC}^{gt} - f_{IHC}^{pred}\|_1, \quad (6)$$

ISA. Beyond feature alignment, we further employ a pixel-level alignment loss, ISA, designed to minimize the ℓ_1 reconstruction error between the predicted IHC image \hat{X}_{IHC}^{pred} and its registered ground-truth counterpart, X_{IHC} . Formally,

$$\mathcal{L}_{ISA} = \|X_{IHC} - \hat{X}_{IHC}^{pred}\|_1, \quad (7)$$

The Translator \mathcal{T} is jointly trained using both constraints:

$$\mathcal{L}_{trans} = \mathcal{L}_{LSA} + \lambda_{trans} \mathcal{L}_{ISA}, \quad (8)$$

where λ_{trans} balances latent-level alignment and image-level spatial fidelity, respectively.

D. Visual Autoregressive Generation via Structural Conditioning

Unlike existing autoregressive models that operate unconditionally or rely on weak semantic cues such as class labels [17], PAINT performs structure-conditioned synthesis to address anatomically implausible layouts in cross-modal generation. Specifically, f_{IHC}^{pred} , computed according to Eq. 5, serves as a spatial anchor, guiding the generation of molecular staining patterns that are strictly aligned with the tissue morphology present in the input H&E image. Based on f_{IHC}^{pred} , two complementary conditioning signals can be derived as expected to guide the generation process: a global context

vector for appearance modulation and a spatially grounded start map for geometry-aware autoregressive initialization.

Global Context Formulation. To capture global representations, global average pooling is applied to $f_{\text{IHC}}^{\text{pred}}$, yielding f_{global} , which is injected into the VAR Transformer via Adaptive Layer Normalization [35], [36], enabling scale-adaptive modulation of feature statistics during generation.

3S-Map S_{start} . To replace the generic learnable start token (e.g., [SOS]) with a spatially explicit initialization, we construct S_{start} directly from the Translator output. Given the aligned feature map $f_{\text{IHC}}^{\text{pred}}$, we downsample it to the resolution of the coarsest scale ($k = 1$) to serve as the initial condition for autoregressive modeling. Formally, S_{start} is computed as:

$$S_{\text{start}} = \text{Interpolate}\left(f_{\text{IHC}}^{\text{pred}}, h_1, w_1\right), \quad (9)$$

where (h_1, w_1) denotes the spatial dimensions of the coarsest scale within the multi-scale hierarchy depicted in Fig. 2(a). This operation ensures that the generation trajectory is initialized with a deterministic, morphology-grounded structural layout derived from the source tissue architecture.

Next-Scale Autoregressive Modeling. PAINT models multi-scale discrete representations via a hierarchical, structure-conditioned autoregressive process, enabling coarse-to-fine generation under explicit anatomical constraints. Let $R = (r_1, r_2, \dots, r_K)$ denote the sequence of discrete token maps across increasing spatial resolutions. The conditional distribution at each scale is defined over all previously generated coarser scales, together with a global structural context extracted from the input:

$$p(R \mid f_{\text{IHC}}^{\text{pred}}) = \prod_{k=1}^K p(r_k \mid r_{<k}, f_{\text{global}}), \quad (10)$$

where $r_{<k}$ denotes tokens generated at coarser scales. To explicitly enforce spatial consistency, the generation is initialized with $r_{<1} = S_{\text{start}}$. This design ensures that each refinement step is jointly conditioned on global semantic context and spatial priors derived from the input H&E image, yielding anatomically coherent and scale-consistent synthesis.

E. Training Objective and Inference

Training Objective. During training, we adopt a teacher-forcing strategy, where ground-truth IHC tokens extracted from the frozen VQ_{IHC} supervise the generation via a token-level cross-entropy loss \mathcal{L}_{CE} applied across all scales. In parallel, the IHC decoder $\mathcal{D}_{\text{IHC}}^{\text{FT}}$ is jointly fine-tuned to enhance image-level fidelity. Specifically, the predicted token hierarchy is decoded into an IHC image $\hat{X}_{\text{IHC}}^{\text{pred}}$, which is constrained to match the ground-truth image X_{IHC} using a combination of pixel-wise reconstruction and adversarial losses. The complete objective is given by

$$\mathcal{L}_{\text{AR}} = \mathcal{L}_{\text{CE}} + \lambda_1 \underbrace{\|X_{\text{IHC}} - \hat{X}_{\text{IHC}}^{\text{pred}}\|_1}_{\mathcal{L}_{\text{pixel}}} + \lambda_2 \mathcal{L}_{\text{adv}}(X_{\text{IHC}}, \hat{X}_{\text{IHC}}^{\text{pred}}), \quad (11)$$

where λ_1 and λ_2 are weighting coefficients.

Inference. At inference time, the autoregressive process is initialized with the 3S-Map and proceeds to sample discrete

tokens scale-by-scale following the learned next-scale distribution. The resulting token pyramid R is decoded to produce the synthesized IHC image using the fine-tuned decoder $\mathcal{D}_{\text{IHC}}^{\text{FT}}$.

IV. EXPERIMENTS

A. Datasets

We evaluated our method on two datasets. **The IHC4BC dataset** [37] comprises multi-patient breast cancer samples stained for ER, PR, HER2, and Ki67. To prevent data leakage and ensure clinically meaningful evaluation, we adopted a patient-level four-fold stratified cross-validation protocol, with folds balanced according to clinical labels. The dataset includes 59 (ER), 52 (HER2), 60 (PR), and 60 (Ki67) patients, corresponding to 26,134, 20,729, 24,971, and 20,668 patch pairs, respectively. **The MIST dataset** [29] provides aligned H&E–IHC image pairs for four clinically relevant breast cancer biomarkers, including estrogen receptor (ER), progesterone receptor (PR), HER2, and Ki67, with a fixed official data split. The training sets contain 4,153 (ER), 4,642 (HER2), 4,139 (PR), and 4,361 (Ki67) image pairs, while each test set includes 1,000 paired samples.

To ensure reliable pixel-level correspondence between H&E and IHC modalities, all raw data in both datasets were first registered using DeeperHistReg [33].

B. Evaluation Metrics

The quality of generated IHC images was assessed on the test sets using peak signal-to-noise ratio (PSNR) [38], structural similarity index measure (SSIM) [39], and learned perceptual image patch similarity (LPIPS) [32], capturing pixel-level fidelity, structural consistency, and perceptual realism, respectively.

On the IHC4BC dataset, we also evaluated the clinical utility of the generated images on downstream classification and regression tasks. We employed specific evaluation pipelines for each biomarker based on standard pathological scoring guidelines [40], [41].

For HER2, the evaluation was formulated as a binary classification task, excluding equivocal cases (score 2+) in accordance with clinical guidelines [40]. Samples with scores {0, 1+} were labeled negative, and those with score 3+ were labeled positive. Performance was evaluated using Accuracy (ACC) and Area Under the ROC Curve (AUC).

For ER, we evaluated both continuous and categorical clinical scores. Nuclei were first stratified into four intensity levels (0, 1+, 2+, 3+) based on diaminobenzidine (DAB) channel intensity thresholds defined by the dataset. Using this stratification, we derived two clinical scores. *H-Score (Regression)*. The H-Score serves as a weighted measure of staining intensity. To ensure robustness to segmentation errors in the generated IHC domain, the total number of nuclei detected in the original H&E image (N_{total}) was used as the denominator, following the dataset protocol. The H-Score is calculated as:

$$\text{H-Score} = \sum_{i=1}^3 \left(i \times \frac{N_{i+}}{N_{\text{total}}} \times 100 \right) \quad (12)$$

TABLE I

QUANTITATIVE COMPARISON ON IHC4BC DATASET. NOTE: THE METRIC HEADERS (ROW 1) APPLY TO THE DATASET COLUMNS GROUPED BELOW THEM (ROW 2). **BOLD** INDICATES BEST, UNDERLINE INDICATES SECOND-BEST.

Method	SSIM \uparrow	PSNR \uparrow	LPIPS \downarrow	SSIM \uparrow	PSNR \uparrow	LPIPS \downarrow
	IHC4BC-ER			IHC4BC-PR		
Pix2pix [10]	0.6904 ± 0.0185	27.9732 ± 1.0074	0.3464 ± 0.0096	0.6907 ± 0.0215	27.5582 ± 0.8272	0.3671 ± 0.0065
CycleGAN [11]	0.6986 ± 0.0126	26.1295 ± 1.0702	0.3185 ± 0.0058	0.6972 ± 0.0211	28.1213 ± 0.9435	0.3340 ± 0.0113
CUT [21]	0.6756 ± 0.0161	25.3983 ± 0.9927	0.3408 ± 0.0042	0.7067 ± 0.0182	28.8566 ± 0.6899	0.3338 ± 0.0098
ASP [29]	0.7000 ± 0.0157	26.8944 ± 1.1434	0.3234 ± 0.0041	0.7342 ± 0.0175	29.8142 ± 0.6957	0.3282 ± 0.0090
PPT [16]	0.6699 ± 0.0194	26.5800 ± 1.2216	0.3403 ± 0.0130	<u>0.7268 ± 0.0162</u>	29.6392 ± 0.6318	0.3398 ± 0.0099
PSPStain [7]	0.6819 ± 0.0079	25.1857 ± 0.6961	0.3292 ± 0.0047	0.7057 ± 0.0152	28.5074 ± 0.4618	0.3253 ± 0.0049
SynDiff [22]	0.7284 ± 0.0134	28.5775 ± 0.7726	0.2862 ± 0.0121	0.7212 ± 0.0197	31.8711 ± 0.7466	0.3395 ± 0.0092
PAINT-s	0.6997 ± 0.0226	29.2288 ± 1.4865	0.2531 ± 0.0071	0.7249 ± 0.0192	31.1782 ± 0.8128	0.2658 ± 0.0063
PAINT	0.7015 ± 0.0207	29.1047 ± 1.4726	0.2362 ± 0.0049	0.7233 ± 0.0211	30.8409 ± 0.8150	0.2608 ± 0.0087
IHC4BC-HER2						
Pix2pix [10]	0.2331 ± 0.0407	14.6460 ± 0.3559	0.5044 ± 0.0146	0.5468 ± 0.0946	24.9537 ± 2.2243	0.3940 ± 0.0147
CycleGAN [11]	0.2730 ± 0.0518	14.0350 ± 0.5465	0.4711 ± 0.0233	0.5560 ± 0.0897	24.6346 ± 2.4722	0.3483 ± 0.0307
CUT [21]	0.2691 ± 0.0519	14.2630 ± 0.5410	0.4646 ± 0.0216	0.5211 ± 0.0830	23.5816 ± 2.0921	0.3610 ± 0.0230
ASP [29]	0.2721 ± 0.0506	14.5904 ± 0.4286	0.4619 ± 0.0200	0.5510 ± 0.0847	24.6968 ± 2.2736	0.3540 ± 0.0247
PPT [16]	0.2550 ± 0.0482	14.6189 ± 0.3877	0.4834 ± 0.0213	<u>0.5589 ± 0.0791</u>	25.1633 ± 2.0750	0.4048 ± 0.0221
PSPStain [7]	0.2702 ± 0.0493	14.4405 ± 0.4251	0.4648 ± 0.0209	0.5502 ± 0.0856	24.1923 ± 2.2107	0.3542 ± 0.0259
SynDiff [22]	<u>0.2747 ± 0.0519</u>	14.4731 ± 0.5457	0.4688 ± 0.0228	0.5537 ± 0.0925	24.8316 ± 2.5527	0.3546 ± 0.0271
PAINT-s	0.2663 ± 0.0428	15.4114 ± 0.2889	0.4299 ± 0.0205	0.5425 ± 0.0885	25.7656 ± 2.3270	0.3210 ± 0.0218
PAINT	0.2792 ± 0.0460	15.3933 ± 0.2714	0.3963 ± 0.0157	0.5592 ± 0.0771	25.3670 ± 2.1536	0.2944 ± 0.0239
IHC4BC-Ki67						

where N_{i+} denotes the count of nuclei with intensity $i+$. The score ranges from 0 to 300. Agreement between predicted and ground-truth H-Scores was quantified using Coefficient of Determination (R^2), Spearman's Rank Correlation, Mean Squared Error (MSE), and Pearson Correlation. *Allred Score (Classification)*. The semi-quantitative Allred Score [42] is calculated as the sum of the Proportion Score (PS) and the Intensity Score (IS), yielding a total score ranging from 0 to 8. Specifically, the PS discretizes the percentage of positive nuclei (p_{pos}) into a six-point scale: 0 ($p_{pos} = 0\%$), 1 ($0\% < p_{pos} < 1\%$), 2 ($1\% \leq p_{pos} \leq 10\%$), 3 ($11\% \leq p_{pos} \leq 33\%$), 4 ($34\% \leq p_{pos} \leq 66\%$), and 5 ($p_{pos} \geq 67\%$). The Intensity Score (IS) represents the average staining intensity of the positive cells, categorized as 0 (None), 1 (Weak), 2 (Intermediate), and 3 (Strong). Performance was reported using ACC, AUC, F1-score, and Cohen's Kappa to reflect both classification accuracy and inter-rater agreement.

For PR and Ki67, we formulated the evaluation of the expression levels as regression tasks. The expression level of PR was evaluated using the H-Score, following the same protocol as ER. Ki67 status was quantified by the percentage of positively stained nuclei relative to the total nuclei count, defined as $\text{Pos\%} = \frac{N_{1+} + N_{2+} + N_{3+}}{N_{total}}$, where all staining intensities (1+ to 3+) are considered positive. For both biomarkers, agreement with ground truth was assessed using R^2 , Spearman's correlation, MSE, and Pearson correlation.

C. Implementation Details

All experiments were implemented in PyTorch and conducted on a cluster equipped with four NVIDIA A100 GPUs.

High-resolution image patches (e.g., 1024×1024) were down-sampled to 256×256 for training and evaluation. The VQ-VAE tokenizer employed a codebook of size 4,096 with a patch size of 16×16 . The standard PAINT model uses 128 base channels and an embedding dimension of 512, while the lightweight variant PAINT-s adopts 64 base channels and an embedding dimension of 256. Adversarial training was performed using a modified three-layer PatchGAN discriminator [10] that aggregates multi-scale intermediate features to provide richer supervision. Optimization was carried out using Adam [43] with an initial learning rate of 1×10^{-4} and a dropout rate of 0.5. Training proceeded in three sequential stages: (a) multi-scale VQ-VAEs were trained for 120 epochs on IHC4BC and 60 epochs on MIST with weights set to $\lambda_p = 1.0$ and $\lambda_{adv} = 0.3$; (b) the cross-modal translation network was trained for 30 epochs on both datasets, utilizing $\lambda_{trans} = 3.0$; and (c) the VAR Transformer was trained for 200 epochs with $\lambda_1 = 1.0$ and $\lambda_2 = 0.3$.

D. Experimental Results

1) *Competing Methods*: We compared PAINT with a comprehensive set of baselines, including general-purpose image translation methods (Pix2Pix [10], CycleGAN [11], CUT [21], and SynDiff [22]) and pathology-specific virtual staining approaches (ASP [29], PPT [16], PSPStain [7], and HistDiST [30]). All baselines were evaluated under identical data splits and preprocessing pipelines.

2) *Results on IHC4BC Dataset*: As presented in Table I, PAINT demonstrates robust performance and consistently outperforms competing methods across the majority of metrics.

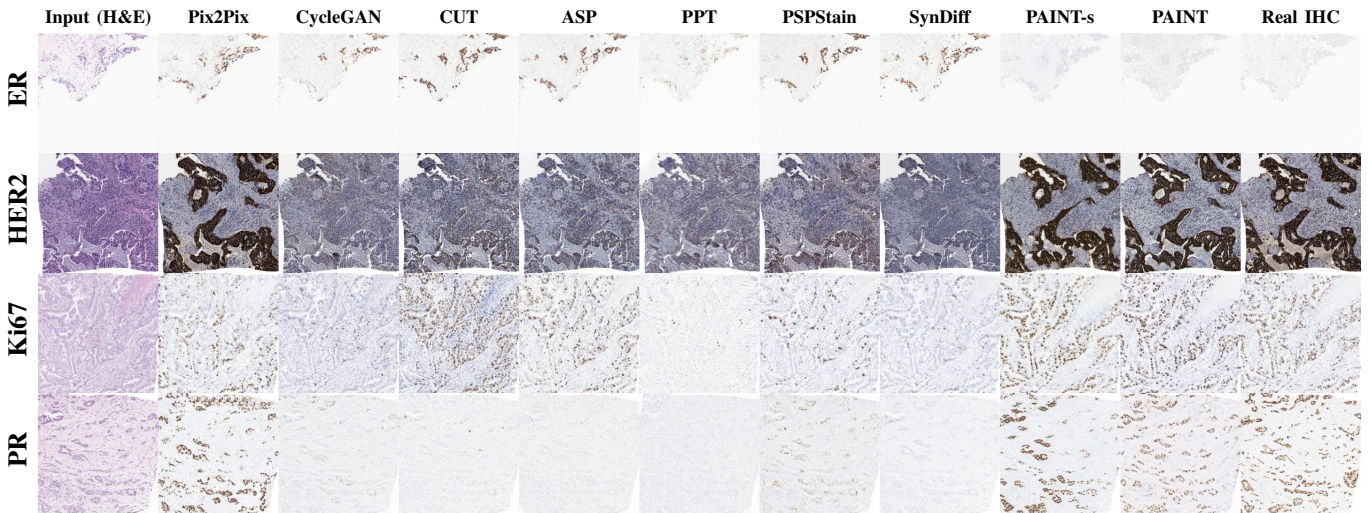


Fig. 3. Visual comparison of ER, HER2, Ki67 and PR generation. From top to bottom, the rows represent different IHC markers. The leftmost column shows the input H&E, and the rightmost column shows the Real IHC.

In terms of perceptual quality, PAINT achieves the lowest LPIPS scores across all four biomarkers, recording 0.2362 for ER. This indicates that our autoregressive modeling approach generates images that are perceptually closer to the ground truth, significantly outperforming the advanced diffusion-based SynDiff (0.2862 on ER) and the GAN-based ASP (0.3234 on ER). Regarding structural and pixel-level fidelity, PAINT consistently ranks within the top two across the majority of SSIM and PSNR evaluations among all competing methods. Even on the IHC4BC-PR subset, PAINT achieves an SSIM score that is highly competitive and comparable to the highest value. These results confirm that PAINT effectively handles the complex staining variations in the IHC4BC dataset, producing high-fidelity images with superior structural details.

3) Results on Downstream Clinical Tasks.: We further evaluated the clinical utility of the generated IHC images on downstream diagnostic tasks using the IHC4BC dataset [37]. Specifically, we utilized the UNI-2 [44] to extract representations from both the predicted IHC images and ground truth H&E slides for all downstream tasks.

HER2 Classification. As shown in Table II, PAINT achieves SOTA performance with an ACC of 0.9753 and an AUC of 0.9902, substantially outperforming all competing methods, such as Pix2Pix (ACC: 0.8948) and CycleGAN (ACC: 0.8093). This demonstrates that PAINT reliably captures the membrane staining patterns necessary for accurate HER2 status determination.

ER Quantification. For ER assessment, PAINT shows the strongest agreement with ground-truth H-Scores, achieving a Pearson correlation of 0.8664 and an R^2 of 0.7354 (Table III). In contrast, conventional GANs like CycleGAN and CUT struggle to capture the correct staining intensity, yielding significantly lower R^2 values. In Allred Score evaluation, PAINT also attains the highest accuracy for both proportion (0.6313) and intensity (0.7635) components, surpassing the second-best method Pix2Pix by significant margins. This confirms that our coarse-to-fine generation accurately captures both the spatial distribution (proportion) and the pixel-level depth (intensity)

TABLE II
QUANTITATIVE CLASSIFICATION PERFORMANCE ON THE IHC4BC-HER2+HE DATASET. **BOLD** INDICATES THE BEST RESULTS, AND UNDERLINE INDICATES THE SECOND-BEST.

Method	ACC \uparrow	AUC \uparrow
H&E	0.8025 \pm 0.0679	0.8436 \pm 0.0987
Pix2pix [10]	<u>0.8948 \pm 0.0386</u>	<u>0.9370 \pm 0.0203</u>
CycleGAN [11]	0.8093 \pm 0.0777	0.8414 \pm 0.1076
CUT [21]	0.8118 \pm 0.0693	0.8592 \pm 0.0786
ASP [29]	0.8206 \pm 0.0569	0.8710 \pm 0.0542
PPT [16]	0.8103 \pm 0.0736	0.8541 \pm 0.0913
PSPStain [7]	0.8350 \pm 0.0633	0.8814 \pm 0.0555
SynDiff [22]	0.8033 \pm 0.0746	0.8471 \pm 0.0968
PAINT-s	0.8709 \pm 0.0420	0.9212 \pm 0.0301
PAINT	0.9753 \pm 0.0130	0.9902 \pm 0.0072

of nuclear stains.

PR and Ki67 Quantification. The capability of PAINT is further demonstrated on the PR and Ki67. In the challenging PR dataset (see Table IV), where most competitive methods (including CycleGAN, CUT, and SynDiff) failed to establish a predictive correlation (yielding negative R^2 values), PAINT maintained a strong linear relationship with a Pearson correlation of 0.7739 and a positive R^2 of 0.5232. This demonstrates that our model correctly infers nuclear expression levels even in cases with subtle staining variances where other generative models collapse. Finally, for the Ki67 proliferation index, which requires precise counting of positive nuclei, PAINT achieves the highest Pearson correlation of 0.8414 and the lowest MSE (0.0017), highlighting its robustness in tasks requiring accurate counting of positive nuclei.

4) Results on MIST Dataset: As shown in Table VI, PAINT consistently outperforms all competing methods across these biomarkers. Notably, PAINT achieves the highest PSNR for all markers, with significant improvements on PR (16.3104) and Ki67 (16.0698), alongside the best or second-best SSIM, including top performance on the PR (0.2326) and HER2

TABLE III

QUANTITATIVE COMPARISON ON IHC4BC-ER. TOP: METRIC CATEGORIES. BOTTOM: SPECIFIC METRICS. **BOLD** INDICATES BEST, UNDERLINE INDICATES SECOND-BEST.

Method	H_Score				Allred Score		PS		IS	
	R ² ↑	Spearman ↑	MSE ↓	Pearson ↑	ACC ↑	AUC ↑	ACC ↑	AUC ↑	ACC ↑	AUC ↑
H&E	0.5292 ± 0.1895	0.7455 ± 0.1415	919.5912 ± 160.8452	0.7651 ± 0.0830	0.4317 ± 0.0153	0.8297 ± 0.0203	0.5979 ± 0.0370	0.8374 ± 0.0396	0.6582 ± 0.0612	0.8191 ± 0.0280
Pix2Pix [10]	0.6572 ± 0.1584	0.7963 ± 0.0914	654.4841 ± 86.5599	0.8186 ± 0.0850	0.4430 ± 0.0238	0.8492 ± 0.0209	0.5768 ± 0.0397	0.8335 ± 0.0424	0.7088 ± 0.0371	<u>0.8583 ± 0.0277</u>
CycleGAN [11]	0.3772 ± 0.2277	0.6875 ± 0.1249	1238.1280 ± 207.0600	0.6750 ± 0.0914	0.3956 ± 0.0264	0.7998 ± 0.0067	0.5489 ± 0.0403	0.8081 ± 0.0246	0.6344 ± 0.0548	0.8020 ± 0.0197
CUT [21]	0.2325 ± 0.2871	0.6271 ± 0.1255	1527.9083 ± 299.2731	0.5956 ± 0.1043	0.3791 ± 0.0288	0.7851 ± 0.0130	0.5205 ± 0.0393	0.7864 ± 0.0310	0.6238 ± 0.0375	0.7964 ± 0.0264
ASP [29]	0.2917 ± 0.2723	0.6566 ± 0.1300	1404.0151 ± 248.8037	0.6340 ± 0.1021	0.3818 ± 0.0162	0.7880 ± 0.0052	0.5329 ± 0.0394	0.7943 ± 0.0308	0.6166 ± 0.0401	0.7918 ± 0.0187
PPT [16]	0.1066 ± 0.2895	0.5723 ± 0.0983	1813.8149 ± 450.2535	0.5103 ± 0.0889	0.3437 ± 0.0275	0.7349 ± 0.0115	0.4879 ± 0.0170	0.7486 ± 0.0266	0.5642 ± 0.0531	0.7406 ± 0.0239
PSPStain [7]	0.3860 ± 0.2184	0.6981 ± 0.1046	1243.4932 ± 346.5706	0.6751 ± 0.0923	0.4000 ± 0.0258	0.7918 ± 0.0138	0.5503 ± 0.0344	0.7985 ± 0.0226	0.6536 ± 0.0524	0.8175 ± 0.0241
SynDiff [22]	0.4914 ± 0.2109	0.7356 ± 0.1120	988.7520 ± 123.9860	0.7429 ± 0.0921	0.4142 ± 0.0136	0.8192 ± 0.0127	0.5776 ± 0.0304	0.8260 ± 0.0281	0.6510 ± 0.0474	0.8132 ± 0.0140
PAINT-s	0.6991 ± 0.0983	0.8177 ± 0.0808	617.4735 ± 199.8048	0.8427 ± 0.0557	0.4551 ± 0.0207	0.8459 ± 0.0203	0.6103 ± 0.0460	0.8523 ± 0.0336	0.7159 ± 0.0617	0.8510 ± 0.0083
PAINT	0.7354 ± 0.0496	0.8321 ± 0.0782	572.8870 ± 242.1100	0.8664 ± 0.0261	0.4920 ± 0.0358	0.8699 ± 0.0065	0.6313 ± 0.0286	0.8624 ± 0.0342	0.7635 ± 0.0677	0.8979 ± 0.0250
real IHC	0.8952 ± 0.0404	0.8870 ± 0.0715	214.3521 ± 80.0639	0.9470 ± 0.0211	0.6445 ± 0.0231	0.9395 ± 0.0094	0.7391 ± 0.0301	0.9262 ± 0.0165	0.9062 ± 0.0343	0.9766 ± 0.0090

TABLE IV

QUANTITATIVE COMPARISON ON IHC4BC-PR H_Score AND IHC4BC-Ki67 Positive Percentage Prediction. **BOLD** INDICATES BEST, UNDERLINE INDICATES SECOND-BEST.

Method	IHC4BC-PR H_Score				IHC4BC-Ki67 Positive Percentage			
	R ² ↑	Spearman ↑	MSE ↓	Pearson ↑	R ² ↑	Spearman ↑	MSE ↓	Pearson ↑
H&E	-0.0994 ± 0.2295	0.4057 ± 0.1223	875.9404 ± 440.1256	0.3830 ± 0.0725	0.5970 ± 0.2293	0.7903 ± 0.1335	0.0020 ± 0.0010	0.8163 ± 0.0759
Pix2Pix [10]	0.3807 ± 0.2688	0.4905 ± 0.1083	<u>444.4576 ± 136.0118</u>	0.6765 ± 0.1008	0.4587 ± 0.3458	0.7565 ± 0.1249	0.0026 ± 0.0011	0.7488 ± 0.1044
CycleGAN [11]	-0.0299 ± 0.1911	0.4115 ± 0.0982	845.8080 ± 497.0253	0.3723 ± 0.0728	0.5165 ± 0.3333	0.7769 ± 0.1317	0.0023 ± 0.0010	0.7719 ± 0.1187
CUT [21]	-0.0420 ± 0.2366	0.3909 ± 0.0935	842.6920 ± 480.2599	0.3571 ± 0.0651	0.4663 ± 0.3644	0.7655 ± 0.1328	0.0025 ± 0.0011	0.7592 ± 0.1009
ASP [29]	-0.0981 ± 0.2605	0.3727 ± 0.0916	886.2112 ± 505.5282	0.3256 ± 0.0721	0.4979 ± 0.3447	0.7692 ± 0.1319	0.0023 ± 0.0010	0.7750 ± 0.0976
PPT [16]	-0.0405 ± 0.1780	0.3455 ± 0.0961	846.6899 ± 470.3499	0.2923 ± 0.0536	0.1283 ± 0.7869	0.7124 ± 0.1198	0.0035 ± 0.0010	0.6841 ± 0.0950
PSPStain [7]	0.1501 ± 0.1844	0.4771 ± 0.0856	692.5934 ± 410.0836	0.5004 ± 0.0392	0.4806 ± 0.3401	0.7576 ± 0.1475	0.0025 ± 0.0011	0.7668 ± 0.0873
SynDiff [22]	-0.0925 ± 0.2272	0.4054 ± 0.0938	881.4252 ± 475.0513	0.3545 ± 0.0731	0.5416 ± 0.2973	0.7890 ± 0.1271	<u>0.0022 ± 0.0010</u>	0.7854 ± 0.1031
PAINT-s	<u>0.3872 ± 0.2341</u>	<u>0.5593 ± 0.0915</u>	453.2665 ± 170.3116	<u>0.6936 ± 0.0627</u>	<u>0.5612 ± 0.2228</u>	0.7796 ± 0.1170	0.0023 ± 0.0011	<u>0.7906 ± 0.0741</u>
PAINT	0.5232 ± 0.1965	0.6006 ± 0.0802	379.2940 ± 239.0373	0.7739 ± 0.0526	0.6819 ± 0.1463	<u>0.7833 ± 0.1593</u>	0.0017 ± 0.0008	0.8414 ± 0.0626
real IHC	0.8732 ± 0.0372	0.7152 ± 0.0699	107.1590 ± 79.9160	0.9428 ± 0.0155	0.8819 ± 0.0697	0.8338 ± 0.1825	0.0006 ± 0.0002	0.9452 ± 0.0325

(0.1983) subsets. In terms of perceptual quality, PAINT also demonstrates superior performance with the lowest LPIPS scores across all biomarkers, achieving 0.4865 for HER2, surpassing the competitive baseline ASP (0.5021) by a clear margin. These findings validate the effectiveness of PAINT's autoregressive strategy, which significantly reduces blurring and structural hallucinations, ensuring high-quality generation for both nuclear and membrane staining patterns.

5) *Ablation Study*: Table V summarizes the impact of key designs in PAINT on the ER-IHC4BC dataset (fold 4), including VAR refinement, alignment losses, decoder adaptation, registration, and the multi-scale autoregressive schedule. The following analysis provides detailed insights into these effects.

Effect of VAR Refinement. Removing the VAR-based refinement stage (w/o VAR) reduces PAINT to directly decoding the Translator output with decoder fine-tuning, but without the Visual autoregressive refinement step. Compared to the full PAINT model with VAR, performance decreases, with SSIM dropping from 0.7321 to 0.6668, and PSNR decreasing from 31.2594 to 13.9647. These results underscore the importance of the refinement stage in improving reconstruction fidelity and perceptual quality.

Effect of \mathcal{L}_{LSA} and \mathcal{L}_{ISA} . Both objectives are involved in shaping the 3S-Map S_{start} . Specifically, enabling \mathcal{L}_{LSA} dramatically improves SSIM from 0.6109 to 0.7321 and PSNR from 19.8506 to 31.2594, while reducing LPIPS from 0.3171 to 0.2402. Similarly, introducing \mathcal{L}_{ISA} increases SSIM from 0.6046 to 0.7321 and PSNR from 17.9799 to 31.2594, with

a corresponding drop in LPIPS from 0.3293 to 0.2402. These results indicate that incorporating spatial alignment cues into S_{start} substantially enhances generation quality by strengthening spatial correspondence between H&E and IHC.

TABLE V

ABLATION STUDY OF PAINT ON THE ER-IHC4BC DATASET (FOLD4). WE INVESTIGATE THE IMPACT OF DIFFERENT LOSS COMPONENTS AND SCALE CONFIGURATIONS. THE BEST RESULTS ARE HIGHLIGHTED IN **BOLD**.

Method / Configuration	SSIM ↑	PSNR ↑	LPIPS ↓
Component Effectiveness			
PAINT w/o VAR	0.6668	13.9647	0.4674
PAINT w/o \mathcal{L}_{LSA}	0.6109	19.8506	0.3171
PAINT w/o \mathcal{L}_{ISA}	0.6046	17.9799	0.3293
PAINT w/o \mathcal{D}_{IHC}^{FT}	0.6571	18.5512	0.4507
PAINT w/o \mathcal{L}_{adv}	0.6829	22.8388	0.3546
PAINT w/o \mathcal{L}_{pixel}	0.6765	27.0371	0.2801
PAINT w/o f_{global}	0.7128	30.7752	0.2493
PAINT w/o Multi-scale	0.7078	26.7970	0.3718
PAINT w/o Registration	0.6726	29.6429	0.3104
Scale Configurations (with all components enabled)			
Scales: (1-16 dense)	0.7236	31.0121	0.2466
Scales: (1, 2, 4, 8, 16)	0.6832	28.2692	0.3322
PAINT: (8-16)	0.7321	31.2594	0.2402

Note: In the "w/o \mathcal{D}_{IHC}^{FT} " variant, the decoder is frozen.

Effect of Decoder Fine-tuning and Loss Design. The contribution of task-specific decoder adaptation and loss objectives

TABLE VI

QUANTITATIVE COMPARISON ACROSS FOUR IHC DATASETS: MIST-ER, MIST-PR, MIST-HER2, AND MIST-Ki67. **BOLD** INDICATES BEST RESULTS, AND UNDERLINE INDICATES SECOND-BEST RESULTS.

Method	MIST-ER			MIST-PR			MIST-HER2			MIST-Ki67		
	SSIM ↑	PSNR ↑	LPIPS ↓	SSIM ↑	PSNR ↑	LPIPS ↓	SSIM ↑	PSNR ↑	LPIPS ↓	SSIM ↑	PSNR ↑	LPIPS ↓
Pix2pix [10]	0.1802	15.2513	0.5249	0.1817	15.3299	0.5168	0.1580	15.1582	0.5253	0.1734	15.0570	0.5192
CycleGAN [11]	0.2183	14.7145	0.5065	0.2201	14.8420	0.5135	0.1897	14.6820	0.5185	0.2067	14.9717	0.5107
CUT [21]	0.2055	14.4950	0.5100	0.2101	14.5126	0.5075	0.1668	13.7156	0.5337	0.2071	14.8732	0.5034
ASP [29]	0.2209	15.4460	<u>0.4994</u>	0.2113	<u>15.3521</u>	<u>0.4889</u>	0.1915	<u>15.5460</u>	<u>0.5021</u>	0.2061	<u>15.7310</u>	<u>0.4995</u>
PPT [16]	0.2061	<u>15.5203</u>	0.5373	0.2114	15.1567	0.5245	0.1791	14.5031	0.5437	0.1987	14.5261	0.5268
PSPStain [7]	0.2141	14.4162	0.5116	0.2100	14.7608	0.5027	0.1797	14.2899	0.5280	0.2129	15.2507	0.5010
HistDiST [30]	0.1943	14.1084	0.5918	0.2000	13.8957	0.5957	0.1792	13.8214	0.6013	0.1999	14.3815	0.5912
SynDiff [22]	0.2100	14.8838	0.5115	<u>0.2267</u>	14.4295	0.5109	<u>0.1920</u>	13.9540	0.5320	0.2176	15.1106	0.5102
PAINT-s	0.2205	15.8477	0.4724	<u>0.2326</u>	16.3104	0.4741	0.1983	15.8843	0.4865	0.2161	16.0698	0.4700

is validated by the ablations on $\mathcal{D}_{\text{IHC}}^{\text{FT}}$, \mathcal{L}_{adv} , and $\mathcal{L}_{\text{pixel}}$. Freezing the IHC decoder (w/o $\mathcal{D}_{\text{IHC}}^{\text{FT}}$) in Fig. 2(c) leads to inferior performance (SSIM: 0.6571; PSNR: 18.5512; LPIPS: 0.4507), demonstrating that decoder adaptation is critical for faithfully rendering the learned latent representation into realistic IHC appearance. In addition, removing \mathcal{L}_{adv} noticeably degrades synthesis quality (SSIM: 0.6829; PSNR: 22.8388), indicating that adversarial supervision is essential for enhancing realism and reducing perceptual discrepancy. Similarly, removing $\mathcal{L}_{\text{pixel}}$ causes a clear drop in reconstruction fidelity (SSIM: 0.6765; PSNR: 27.0371), suggesting that pixel-wise regression provides a strong low-level anchor for stable synthesis.

Effect of Global Conditioning. The global conditioning signal f_{global} provides patch-level contextual guidance and is injected into the generator via AdaLN-based modulation to regulate global staining style and intensity. The benefit of this design is clear when comparing PAINT w/o f_{global} with the full model. Adding f_{global} improves SSIM from 0.7128 to 0.7321 (+0.0193) and PSNR from 30.7752 to 31.2594 (+0.4842), and reduces LPIPS from 0.2493 to 0.2402 (-0.0091). This indicates that global conditioning helps maintain consistent staining intensity and overall appearance.

Effect of Multi-scale Strategy. The multi-scale strategy in PAINT is implemented via residual quantization to progressively decompose histological structures from coarse to fine scales. Its impact is evident when comparing PAINT w/o *Multi-scale* to the full model, where enabling multi-scale modeling improves PSNR by 4.46 (26.7970→31.2594) and reduces LPIPS by 0.13 (0.3718→0.2402). These improvements highlight the benefit of multi-scale decomposition in capturing complex histological patterns and supporting robust high-resolution synthesis with enhanced perceptual quality.

Effect of Registration. To evaluate the necessity of explicit H&E-IHC alignment, we remove the registration module. The w/o *Registration* variant performs worse (SSIM: 0.6726; PSNR: 29.6429; LPIPS: 0.3104), while enabling registration improves SSIM to 0.7321 (+0.0595) and PSNR to 31.2594 (+1.6165), and reduces LPIPS to 0.2402 (-0.0702). These results indicate that correcting spatial misalignment reduces supervision noise and is a prerequisite for stable learning of cross-modal correspondence.

Impact of Autoregressive Scale Configurations. We finally investigate different scale schedules (bottom of Table V). A sparse progression (1, 2, 4, 8, 16) is suboptimal (SSIM: 0.6832; PSNR: 28.2692; LPIPS: 0.3322), implying insufficient intermediate refinement. Using dense scales from extremely coarse resolutions (1–16 dense) performs better (SSIM: 0.7236; PSNR: 31.0121; LPIPS: 0.2466) but still lags behind the proposed setting. Specifically, PAINT (8–16 dense) achieves SSIM = 0.7321, PSNR = 31.2594, and LPIPS = 0.2402, showing gains of +0.0085 SSIM, +0.2473 PSNR, and -0.0064 LPIPS compared to the second best schedule (1–16 dense). This suggests that initializing with the 3S-Map at mid-resolution and progressively refining with dense scales strikes the best balance between stability and detail recovery.

V. CONCLUSION

In this paper, we presented PAINT, a pathology-aware visual autoregressive framework that rethinks virtual IHC as a structure-conditioned generation task rather than a deterministic translation problem. By addressing the inherently underdetermined relationship between H&E morphology and IHC molecular expression, PAINT effectively mitigates the structural hallucinations prevalent in current approaches. A key innovation of our method is the 3S-Map, which enforces dual constraints in both latent and image spaces. This design effectively creates a morphology-grounded structural prior, preventing spatial drift and ensuring that generated molecular signals remain anatomically coherent with the underlying tissue architecture. Comprehensive evaluations on the IHC4BC and MIST datasets demonstrate PAINT’s superiority over SOTA methods in generating high-fidelity, structurally accurate, and clinically viable staining patterns. While the multi-scale quantization inherent to VQ-VAE frameworks introduces a slight information bottleneck regarding fine-grained reconstruction, our results confirm that structure-guided autoregressive modeling offers a robust and principled direction for the future of computational pathology.

REFERENCES

- [1] M. N. Gurcan, L. E. Boucheron, A. Can, A. Madabhushi, N. M. Rajpoot, and B. Yener, “Histopathological image analysis: A review,” *IEEE reviews in biomedical engineering*, vol. 2, pp. 147–171, 2009.

[2] M. K. K. Niazi, A. V. Parwani, and M. N. Gurcan, "Digital pathology and artificial intelligence," *The lancet oncology*, vol. 20, no. 5, pp. e253–e261, 2019.

[3] Y. Rivenson, H. Wang, Z. Wei, Y. Zhang, H. Gunaydin, and A. Ozcan, "Deep learning-based virtual histology staining using auto-fluorescence of label-free tissue," *arXiv preprint arXiv:1803.11293*, 2018.

[4] P. Ghahremani, J. Marino, R. Dodds, and S. Nadeem, "Deeplif: An online platform for quantification of clinical pathology slides," in *Proceedings of the IEEE/CVF Conference on Computer Vision and Pattern Recognition*, 2022, pp. 21 399–21 405.

[5] M. Lu, T. Wang, and Y. Xia, "Multi-modal pathological pre-training via masked autoencoders for breast cancer diagnosis," in *International Conference on Medical Image Computing and Computer-Assisted Intervention*. Springer, 2023, pp. 457–466.

[6] B. He, L. Bergenstråhlé, L. Stenbeck, A. Abid, A. Andersson, Å. Borg, J. Maaskola, J. Lundeberg, and J. Zou, "Integrating spatial gene expression and breast tumour morphology via deep learning," *Nature biomedical engineering*, vol. 4, no. 8, pp. 827–834, 2020.

[7] F. Chen, R. Zhang, B. Zheng, Y. Sun, J. He, and W. Qin, "Pathological semantics-preserving learning for h&e-to-ihc virtual staining," in *International Conference on Medical Image Computing and Computer-Assisted Intervention*. Springer, 2024, pp. 384–394.

[8] H. Tian, T. Lv, J. Fan, D. Pan, L. Li, and X. Pan, "Coarse-to-fine medical image translation by incorporating deterministic guidance and probabilistic refinement," in *International Conference on Medical Image Computing and Computer-Assisted Intervention*. Springer, 2025, pp. 128–137.

[9] C. L. Srinidhi, O. Ciga, and A. L. Martel, "Deep neural network models for computational histopathology: A survey," *Medical image analysis*, vol. 67, p. 101813, 2021.

[10] P. Isola, J.-Y. Zhu, T. Zhou, and A. A. Efros, "Image-to-image translation with conditional adversarial networks," in *Proceedings of the IEEE conference on computer vision and pattern recognition*, 2017, pp. 1125–1134.

[11] J.-Y. Zhu, T. Park, P. Isola, and A. A. Efros, "Unpaired image-to-image translation using cycle-consistent adversarial networks," in *Proceedings of the IEEE international conference on computer vision*, 2017, pp. 2223–2232.

[12] J. P. Cohen, M. Luck, and S. Honari, "Distribution matching losses can hallucinate features in medical image translation," in *International conference on medical image computing and computer-assisted intervention*. Springer, 2018, pp. 529–536.

[13] S. Bhadra, V. A. Kelkar, F. J. Brooks, and M. A. Anastasio, "On hallucinations in tomographic image reconstruction," *IEEE transactions on medical imaging*, vol. 40, no. 11, pp. 3249–3260, 2021.

[14] M. Tivnan, S. Yoon, Z. Chen, X. Li, D. Wu, and Q. Li, "Hallucination index: An image quality metric for generative reconstruction models," in *International Conference on Medical Image Computing and Computer-Assisted Intervention*. Springer, 2024, pp. 449–458.

[15] S. Dayarathna, Y. Wu, J. Cai, T.-T. Wong, M. Law, K. T. Islam, H. Peiris, and Z. Chen, "Mu-diff: a mutual learning diffusion model for synthetic mri with application for brain lesions," *npj Artificial Intelligence*, vol. 1, no. 1, p. 11, 2025.

[16] W. Zhang, T. H. Hui, P. Y. Tse, F. Hill, C. Lau, and X. Li, "High-resolution medical image translation via patch alignment-based bidirectional contrastive learning," in *International Conference on Medical Image Computing and Computer-Assisted Intervention*. Springer, 2024, pp. 178–188.

[17] K. Tian, Y. Jiang, Z. Yuan, B. Peng, and L. Wang, "Visual autoregressive modeling: Scalable image generation via next-scale prediction," *Advances in neural information processing systems*, vol. 37, pp. 84 839–84 865, 2024.

[18] A. Razavi, A. Van den Oord, and O. Vinyals, "Generating diverse high-fidelity images with vq-vae-2," *Advances in neural information processing systems*, vol. 32, 2019.

[19] S. Bengio, O. Vinyals, N. Jaitly, and N. Shazeer, "Scheduled sampling for sequence prediction with recurrent neural networks," *Advances in neural information processing systems*, vol. 28, 2015.

[20] Y. Wu, T. Song, Z. Wu, J. Ye, Z. Ge, Z. Chen, and J. Cai, "Codebrain: Imputing any brain mri via modality-and instance-specific codes," *arXiv preprint arXiv:2501.18328*, 2025.

[21] T. Park, A. A. Efros, R. Zhang, and J.-Y. Zhu, "Contrastive learning for unpaired image-to-image translation," in *European conference on computer vision*. Springer, 2020, pp. 319–345.

[22] M. Özbeý, O. Dalmaz, S. U. Dar, H. A. Bedel, Ş. Öztürk, A. Güngör, and T. Cukur, "Unsupervised medical image translation with adversarial diffusion models," *IEEE Transactions on Medical Imaging*, vol. 42, no. 12, pp. 3524–3539, 2023.

[23] R. Rombach, A. Blattmann, D. Lorenz, P. Esser, and B. Ommer, "High-resolution image synthesis with latent diffusion models," in *Proceedings of the IEEE/CVF conference on computer vision and pattern recognition*, 2022, pp. 10 684–10 695.

[24] P. Esser, R. Rombach, and B. Ommer, "Taming transformers for high-resolution image synthesis," in *Proceedings of the IEEE/CVF conference on computer vision and pattern recognition*, 2021, pp. 12 873–12 883.

[25] J. Yu, X. Li, J. Y. Koh, H. Zhang, R. Pang, J. Qin, A. Ku, Y. Xu, J. Baldridge, and Y. Wu, "Vector-quantized image modeling with improved vqgan," *arXiv preprint arXiv:2110.04627*, 2021.

[26] Y.-J. Chen, S.-I. Cheng, W.-C. Chiu, H.-Y. Tseng, and H.-Y. Lee, "Vector quantized image-to-image translation," in *European Conference on Computer Vision*. Springer, 2022, pp. 440–456.

[27] N. Parmar, A. Vaswani, J. Uszkoreit, L. Kaiser, N. Shazeer, A. Ku, and D. Tran, "Image transformer," in *International conference on machine learning*. PMLR, 2018, pp. 4055–4064.

[28] A. Van Den Oord, N. Kalchbrenner, and K. Kavukcuoglu, "Pixel recurrent neural networks," in *International conference on machine learning*. PMLR, 2016, pp. 1747–1756.

[29] F. Li, Z. Hu, W. Chen, and A. Kak, "Adaptive supervised patchnce loss for learning h&e-to-ihc stain translation with inconsistent groundtruth image pairs," in *International Conference on Medical Image Computing and Computer-Assisted Intervention*. Springer, 2023, pp. 632–641.

[30] E. Großkopf, V. Bunde, M. Hosseinzadeh, and H. Lensch, "Hist-dist: Histopathological diffusion-based stain transfer," *arXiv preprint arXiv:2505.06793*, 2025.

[31] J. Han, J. Liu, Y. Jiang, B. Yan, Y. Zhang, Z. Yuan, B. Peng, and X. Liu, "Infinity: Scaling bitwise autoregressive modeling for high-resolution image synthesis," in *Proceedings of the Computer Vision and Pattern Recognition Conference*, 2025, pp. 15 733–15 744.

[32] R. Zhang, P. Isola, A. A. Efros, E. Shechtman, and O. Wang, "The unreasonable effectiveness of deep features as a perceptual metric," in *Proceedings of the IEEE conference on computer vision and pattern recognition*, 2018, pp. 586–595.

[33] M. Wodzinski, N. Marini, M. Atzori, and H. Müller, "Deeperhistreg: robust whole slide images registration framework," *arXiv preprint arXiv:2404.14434*, 2024.

[34] O. Ronneberger, P. Fischer, and T. Brox, "U-net: Convolutional networks for biomedical image segmentation," in *International Conference on Medical image computing and computer-assisted intervention*. Springer, 2015, pp. 234–241.

[35] X. Huang and S. Belongie, "Arbitrary style transfer in real-time with adaptive instance normalization," in *Proceedings of the IEEE international conference on computer vision*, 2017, pp. 1501–1510.

[36] W. Peebles and S. Xie, "Scalable diffusion models with transformers," in *Proceedings of the IEEE/CVF international conference on computer vision*, 2023, pp. 4195–4205.

[37] A. Akbarnejad, N. Ray, P. J. Barnes, and G. Bigras, "Predicting ki67, er, pr, and HER2 statuses from h&e-stained breast cancer images," *arXiv preprint arXiv:2308.01982*, 2023.

[38] B. Jähne, *Digital image processing*. Springer, 2005.

[39] Z. Wang, A. C. Bovik, H. R. Sheikh, and E. P. Simoncelli, "Image quality assessment: from error visibility to structural similarity," *IEEE transactions on image processing*, vol. 13, no. 4, pp. 600–612, 2004.

[40] A. C. Wolff, M. E. H. Hammond, K. H. Allison, B. E. Harvey, P. B. Mangu, J. M. Bartlett, M. Bilous, I. O. Ellis, P. Fitzgibbons, W. Hanna *et al.*, "Human epidermal growth factor receptor 2 testing in breast cancer: American society of clinical oncology/college of american pathologists clinical practice guideline focused update," *Archives of pathology & laboratory medicine*, vol. 142, no. 11, pp. 1364–1382, 2018.

[41] K. H. Allison, M. E. H. Hammond, M. Dowsett, S. E. McKernin, L. A. Carey, P. L. Fitzgibbons, D. F. Hayes, S. R. Lakhani, M. Chavez-MacGregor, J. Perlmutter *et al.*, "Estrogen and progesterone receptor testing in breast cancer: Asco/cap guideline update," *Journal of Clinical Oncology*, vol. 38, no. 12, pp. 1346–1366, 2020.

[42] M. F. Ahmad Fauzi, W. S. H. M. Wan Ahmad, M. F. Jamaluddin, J. T. H. Lee, S. Y. Khor, L. M. Looi, F. S. Abas, and N. Aldahoul, "Allred scoring of er-ihc stained whole-slide images for hormone receptor status in breast carcinoma," *Diagnostics*, vol. 12, no. 12, p. 3093, 2022.

[43] D. P. Kingma and J. Ba, "A method for stochastic optimization," *arXiv preprint arXiv:1412.6980*, vol. 1412, no. 6, 2014.

[44] R. J. Chen, T. Ding, M. Y. Lu, D. F. Williamson, G. Jaume, A. H. Song, B. Chen, A. Zhang, D. Shao, M. Shaban *et al.*, "Towards a general-purpose foundation model for computational pathology," *Nature medicine*, vol. 30, no. 3, pp. 850–862, 2024.